PHOTONICS Research

Observation of gapless corner modes of photonic crystal slabs in synthetic translation dimensions

WEN-JIN ZHANG,[1,†] HAO-CHANG MO,[1,†] WEN-JIE CHEN,[1] XIAO-DONG CHEN,[1,*] AND JIAN-WEN DONG[1,2]

[1]*School of Physics & State Key Laboratory of Optoelectronic Materials and Technologies, Sun Yat-sen University, Guangzhou 510275, China*
[2]*e-mail: dongjwen@mail.sysu.edu.cn*
[†]*These authors contributed equally to this work.*
Corresponding author: chenxd67@mail.sysu.edu.cn

Second-order topological photonic crystals support localized corner modes that deviate from the conventional bulk-edge correspondence. However, the frequency shift of corner modes spanning the photonic band gap has not been experimentally reported. Here, we observe the gapless corner modes of photonic crystal slabs within a parameter space by considering translation as an additional synthetic dimension. These corner modes, protected by topological pumping in synthetic translation dimensions, are found to exist independently of the specific corner configuration. The gapless corner modes are experimentally imaged via the near-field scanning measurement and validated numerically by full-wave simulations. We propose a topological rainbow with gradient translation, demonstrating the ability to extract and separate specific frequency components of light into different spatial locations. Our work contributes to the advancement of topological photonics and provides valuable insights into the exploration of gapless corner modes in synthetic dimensions. © 2024 Chinese Laser Press

1. INTRODUCTION

Topological photonic crystals (PCs) have emerged as a rapidly growing field of research in the past few years, holding great potential for revolutionizing the way we mold the flow of light [1–9]. A key characteristic of topological PCs is the presence of topologically protected boundary modes localized at the crystal's boundary. According to the conventional bulk-edge correspondence, these topological boundary modes are generally one dimension lower than the topological systems themselves. For instance, one-dimensional topological systems host zero-dimensional topological modes [10–12], while two-dimensional topological systems host one-dimensional topological edge modes [13–15]. These topological boundary modes exhibit robustness against various defects and perturbations, rendering them highly resilient. However, certain perturbations targeting their topological protection mechanisms can compromise their robustness. Strong symmetry-breaking or large-scale structural deformation is examples of such perturbations that can disrupt the robustness of the topological modes. For instance, edge modes of valley photonic crystals are resilient against perturbations that do not mix the two valleys [16,17]. On the contrary, the sidewall roughness of valley photonic crystals can introduce backscattering and impact the robustness of topological edge modes [18].

Recent advancements have unveiled a novel class of topological phases known as higher-order topological phases, which deviate the traditional bulk-edge correspondence [19–23]. In contrast to conventional topological materials, the boundary modes of higher-order topological materials are more than one dimension lower than the bulk. For example, two-dimensional second-order topological photonic crystals (STPCs) can host zero-dimensional corner modes [24–36]. These corner modes are localized at the intersection of two lower-dimensional boundaries within the STPCs and hold significant promise for various applications, including on-chip cavities [37–39], advanced lasers [40,41], and nonlinear optics [42–44]. However, in realistic PC cavities, there are some perturbations causing the frequency shifts of the corner modes. For example, the translation of rods or holes in PCs is a common fabrication error during the fabrication and also induces frequency shifts of the corner modes [41,45]. Although the translation dependent frequency shift is hard to predict, a recent theoretical proposal has shown that frequency shift of corner modes spanning the entire band gap (i.e., gapless corner modes) can be achieved by considering the translation as an additional synthetic dimension [46]. Note that the introduction of synthetic dimensions [47–49] in photonic systems enriches the exploration of topological phase of light in higher-dimensional space beyond three-dimensional real-space [50–56]. The topology in synthetic translation space ensures the gapless modes, e.g., the gapless boundary modes from two-dimensional synthetic space [57], and gapless corner

and dislocation modes from four-dimensional synthetic space [46]. These gapless modes facilitate the topological rainbow to separate different topological modes into distinct locations [58,59]. However, the gapless corner modes in Ref. [46] are based on ideal two-dimensional PCs without direct experimental evidence. Here, we observe the gapless frequency shift of corner modes in the PC slab. The experimental paradigm developed for the PC slab is adaptable to optical frequencies, offering promising avenues for frequency-tunable nanocavity. As a practical application, we propose a topological rainbow device with a PC slab, which can configure the corner modes of different frequencies at different locations.

In this work, the PC slab consists of periodic ceramic square-rods placed on a metallic substrate. By introducing the translation $(\Delta x, \Delta y)$ into the PC slab, we can tune the frequency of the corner mode, thus demonstrating the existence of the gapless corner mode in synthetic translation dimensions. To validate our findings, we employ the near-field scanning measurements to experimentally image the localized corner modes. We systematically explore and image corner modes in PC slabs under different translational deformations, confirming the frequency shift of the corner mode. All experimental results are further supported by full-wave simulations, ensuring the reliability of our findings. Our findings demonstrate the potential for the flexible

frequency modulation of corner modes in synthetic translation dimensions.

2. GAPLESS CORNER MODES IN SYNTHETIC TRANSLATION DIMENSIONS

To illustrate the presence of corner modes and their gapless dispersion in synthetic translation dimensions, we first consider the corner formed between a two-dimensional (2D) STPC and an ordinary photonic crystal (OPC) [Fig. 1(a)]. The unit cell of the STPC consists of four square-rods with a side length of 3.5 mm. The distances between two neighboring rods in the in-plane directions are $d_x = d_y = 14.5$ mm. In contrast, the unit cell of the OPC consists of a square-rod with a side length of 7 mm. The lattice constant of both PCs is $a = 18$ mm, and the relative permittivity of the rod is 5.9. The topology of these two PCs is given by the 2D Zak phase $\boldsymbol{Z} = (Z_x, Z_y)$ [25,26]:

$$Z_j = \int dk_x dk_y \text{Tr}[\hat{A}(\mathbf{k})], \tag{1}$$

where $j = x$ or y and $\hat{A}_j(\boldsymbol{k}) = i\langle u(\boldsymbol{k})|\partial_{k_j}|u(\boldsymbol{k})\rangle$, with $|u(\boldsymbol{k})\rangle$ being the periodic Bloch function. The 2D Zak phases of the STPC and OPC are (π, π) and $(0, 0)$, respectively, enabling the localized corner modes when the STPC and OPC are placed together to form a corner. The eigenfrequencies of this
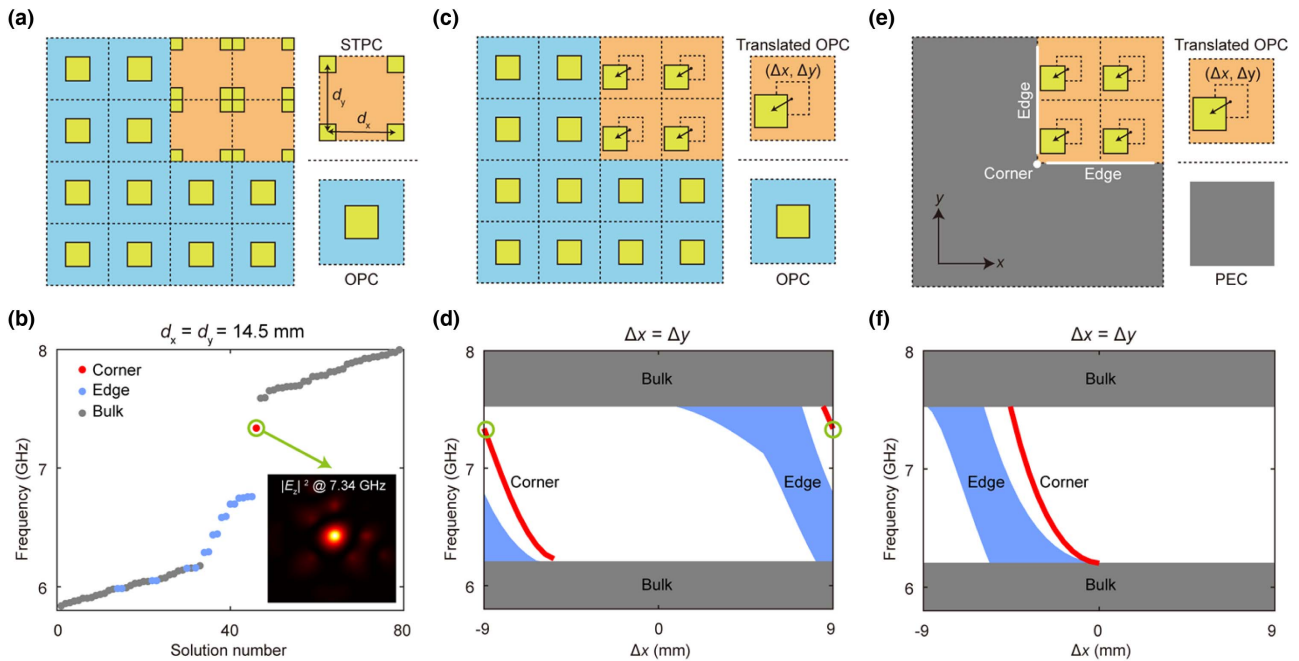

Fig. 1. Corner mode and its gapless dispersion in synthetic translation dimensions. (a) Schematic illustration of the corner between STPC and OPC. Parameters: lattice constant $a = 18$ mm; the side length of square-rod of OPC (blue region) is 7 mm, while that of STPC (orange region) is 3.5 mm; in-plane distances between two neighboring rods in STPC are $d_x = d_y = 14.5$ mm; relative permittivity of rods $\varepsilon_r = 5.9$. (b) Calculated eigenfrequencies of configuration in (a). The corner, edge, and bulk modes are denoted by red, blue, and gray points, respectively. Inset: simulated $|E_z|^2$ field of the corner mode (outlined by a green circle). (c) Schematic illustration of the corner between the translated OPC and the untranslated OPC. All square-rods of the translated OPC are translated away from the center of the unit cell by $(\Delta x, \Delta y)$. (d) The gapless dispersion of corner modes of configuration in (c) when $\Delta x = \Delta y$. Corner modes outlined by two green circles at $\Delta x = \Delta y = -9$ and 9 mm are the same as the corner mode in (b). (e) Schematic illustration of the corner between the translated OPC and PEC to confirm the robustness of the existence of gapless corner modes. (f) The gapless dispersion of corner modes of configuration in (e) when $\Delta x = \Delta y$.

corner configuration are calculated and presented in Fig. 1(b). The corner mode is denoted by the red point, while the edge and bulk modes are denoted by blue and gray points, respectively. The inset of Fig. 1(b) shows the $|E_z|^2$ field of the corner mode, demonstrating strong field confinement at the corner.

The unit cell of the OPC can also be considered to consist of four square-rods with a side length of 3.5 mm and the in-plane distances of $d_x = d_y = 3.5$ mm. As a result, the unit cell of the STPC can be obtained through the unit cell of the OPC by changing the in-plane distances of d_x and d_y from 3.5 mm to 13.5 mm [Fig. 7(b) in Appendix A]. Alternatively, the STPC's unit cell can be obtained by translating the dielectric rod within the OPC along two directions, i.e., Δx and Δy. Note that, when the dielectric rod traverses the unit cell during translation, the patch exiting one boundary re-enters through the corresponding periodic boundary, ensuring the integrity of the entire bulk crystal remains unchanged (Fig. 6 in Appendix A). As the translations Δx and Δy are cyclic and restricted to $[-a/2, a/2]$, they can be considered as two additional Bloch momenta. Combining two original momenta of k_x and k_y, we can define a four-dimensional synthetic $(k_x, \Delta x, k_y, \Delta y)$ space [46]. In contrast to the 2D Zak phase defined within the two-dimensional (k_x, k_y) space, the topological invariant within the four-dimensional $(k_x, \Delta x, k_y, \Delta y)$ space is the second Chern number [60]:

$$C^{(2)} = \frac{1}{32\pi^2} \int \varepsilon_{lmno} B_{lm}(k_x, \Delta x, k_y, \Delta y)$$
$$\times B_{no}(k_x, \Delta x, k_y, \Delta y) \mathrm{d}k_x \mathrm{d}\Delta x \mathrm{d}k_y \mathrm{d}\Delta y, \quad \textbf{(2)}$$

where ε_{lmno} is the Levi-Civita symbol and each index l, m, n, o takes values of k_x, Δx, k_y, or Δy. The second Chern number is nonzero and quantized to be 1, implying the gapless corner modes in synthetic translation dimensions by the bulk-edge correspondence. To see this, we replace the STPC with a translated OPC whose square-rods are all translated away from the center of the unit cell by $(\Delta x, \Delta y)$ [Fig. 1(c)]. For simplicity, we consider the case of $\Delta x = \Delta y$ and calculate the eigenfrequencies of corner modes with different Δx values [denoted by red in Fig. 1(d)]. As Δx varies from -9 to 9 mm, the corner modes bifurcate from the bulk band edge and traverse the entire photonic band gap. It is noteworthy that the corner modes highlighted by two green circles at $\Delta x = \Delta y = -9$ and 9 mm are the same as the corner mode presented in Fig. 1(b). This indicates that the corner mode in the STPC is a lower-dimensional manifestation of gapless corner modes under translational deformation. Note that the term "gapless" used here is related to the synthetic translation dimensions, not the momentum dimension k. The slope of corner mode dispersion is negative, but it only represents the frequency dependence of the corner mode frequency and the translation $(\Delta x, \Delta y)$. In fact, corner modes with tunable frequencies can also be obtained by changing d_x and d_y [Fig. 7(c) in Appendix A]. However, the dispersion under variable d_x and d_y is limited to a small frequency range. We notice that another type of translation, quantified by the parameter g, has been introduced to the STPC to enhance the quality factor of the corner mode [41,45]. Here, g represents the gap distance between the trivial and nontrivial parts of the PC slab, which can be tuned for

creating high-quality topological nanocavities. However, such translation also fails to ensure the gapless frequency shift of corner mode without altering the shape of air holes (or dielectric rods) of STPC. The existence of gapless corner modes is robust and determined by the topological pumping in synthetic translation dimensions [61], which is independent of specific boundary conditions. To further illustrate this point, we replace the OPC with a trivial perfect electric conductor (PEC) [Fig. 1(e)] and calculate its corner mode dispersion as a function of translation [Fig. 1(f)]. Remarkably, gapless corner modes that traverse the entire photonic band gap are still supported when $\Delta x = \Delta y$ (red curve), and the complete frequency diagram of the corner modes in $(\Delta x, \Delta y)$ space is shown in Fig. 8 in Appendix A. When $(\Delta x, \Delta y)$ departs from (0 mm, 0 mm), the corner mode's frequency keeps increasing, and its eigen fields are first extended, then localized, and finally are extended again, showing a crucial characteristic of topological pumping. The frequency shift of corner mode is a boundary effect, but the gapless frequency shift is a topological effect. To clarify this point, we investigate the evolution of the gapless corner modes by adding air layers of different thicknesses weakening the boundary effect (Fig. 9 in Appendix A).

3. REALIZATION ON PHOTONIC CRYSTAL SLABS

To observe gapless corner modes, we implement the above idea in the PC slab that utilizes both the in-plane periodicity and out-of-plane total reflection to confine light in three dimensions [Fig. 2(a)]. The unit cell of the PC slab consists of a dielectric square-rod with the relative permittivity of $\varepsilon_r = 9$ placed on a metallic substrate. The in-plane lattice constant is $a = 18$ mm, and the side length and height of dielectric rods are $b = 7$ mm and $h = 13.5$ mm, respectively. When the relative permittivity is configured from 5.9 to 9, the bulk bands and eigen fields of this PC slab resemble those of the 2D PC presented in Fig. 1 (Fig. 10 in Appendix B), indicating the potential existence of gapless corner modes in the PC slab. To explore this possibility, we construct the "corner" by placing two metallic bars along the x and y directions next to the PC slab. The "corner" wrapped by the OPC should also has gapless corner modes and be more predictable, so we do not perform the observation. We first calculate the eigenfrequencies for the sample with $(\Delta x, \Delta y) = (-2$ mm, -4 mm) [Fig. 2(b)]. Along the frequency axis, the bulk, edge, and corner modes are denoted by gray, blue, and red points, respectively. The frequency range of the band gap is outlined by a cyan rectangle. The $|E_z|^2$ fields at $z = 0$ mm for five representative bulk, edge, and corner modes are shown in Fig. 2(c). These fields show the frequency-dependent mode evolution. The bulk modes extend throughout the crystal, the edge modes propagate along x (or y) direction while being confined along the other direction, and the in-gap corner mode with a frequency of 6.66 GHz is localized in both directions. To achieve gapless corner modes, we translate the PC slab with respect to two static metallic bars. For simplicity, we focus on the representative case of $\Delta x = \Delta y$. Figures 2(d)–2(f) show the eigenfrequencies and $|E_z|^2$ fields of corner modes for the samples with $(\Delta x, \Delta y) = (-3$ mm, -3 mm), $(\Delta x, \Delta y) = (-4$ mm, -4 mm),
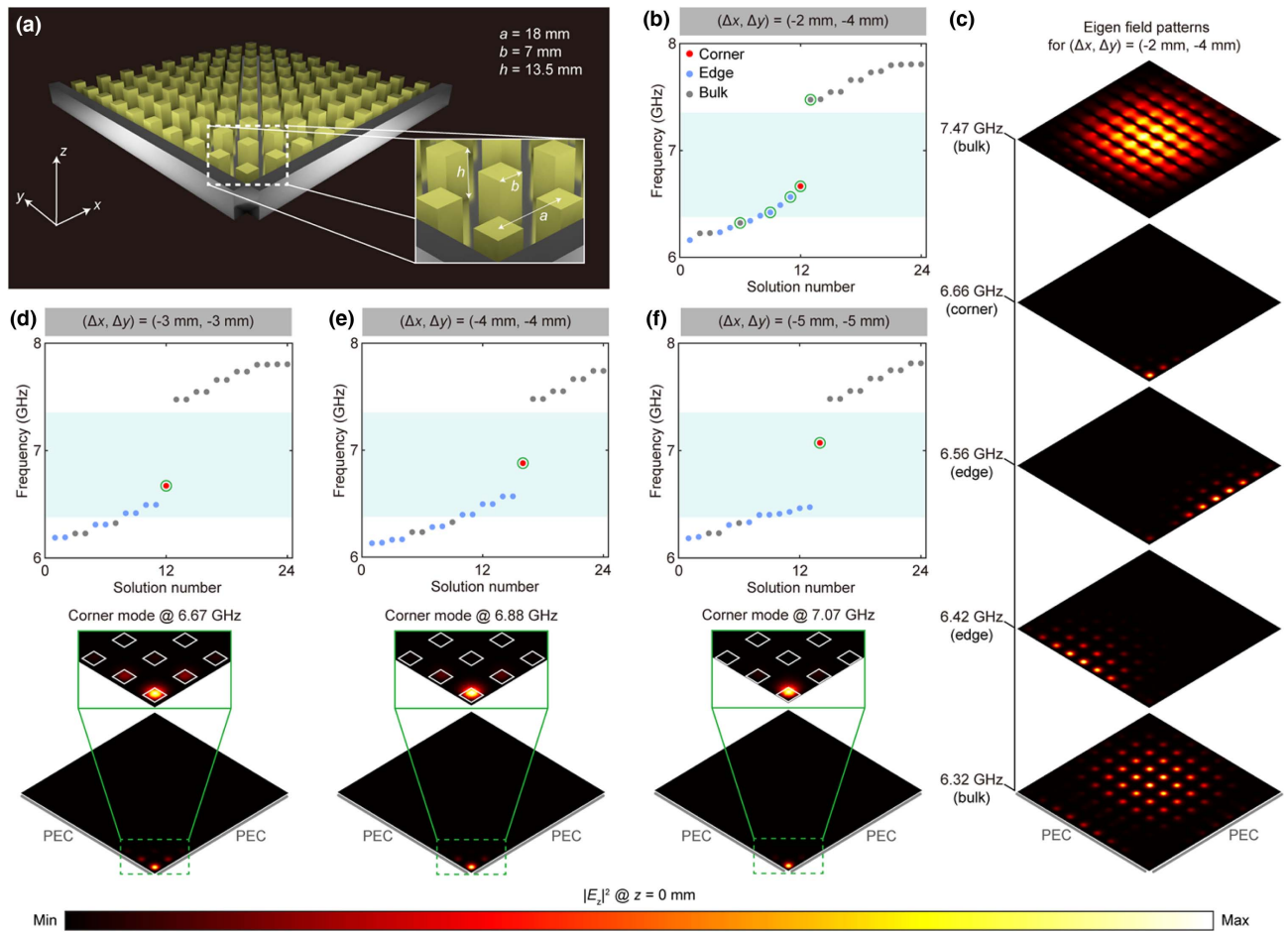
Fig. 2. Realization of gapless corner modes based on PC slab. (a) Schematic illustration of the corner between the PC slab and two metallic bars. Both the PC slab and metallic bars are placed on a metallic substrate. Parameters: lattice constant $a = 18$ mm; in-plane side length of dielectric rods $b = 7$ mm; height of dielectric rods $h = 13.5$ mm; and relative permittivity of dielectric rods $\varepsilon_r = 9$. (b) Calculated eigenfrequencies for the sample with $(\Delta x, \Delta y) = (-2$ mm, -4 mm$)$. The cyan region represents the bulk band gap of PC slab. The eigen modes whose $|E_z|^2$ fields will be shown in (c) are outlined by circles. (c) $|E_z|^2$ fields at $z = 0$ mm for bulk, edge, and corner modes in (b). (d)–(f) Calculated eigenfrequencies and $|E_z|^2$ fields of the corner modes for the sample with $(\Delta x, \Delta y) = (-3$ mm, -3 mm$)$, $(-4$ mm, -4 mm$)$, and $(-5$ mm, -5 mm$)$.

and $(\Delta x, \Delta y) = (-5$ mm, -5 mm$)$. In these three samples, corner modes are found within the bulk band gap and localized around the corner. In addition, the frequencies of corner modes increase from 6.67 GHz to 6.88 GHz to 7.07 GHz as Δx decreases, showcasing the manifestation of gapless corner modes in PC slabs.

4. EXPERIMENTAL OBSERVATION

The PC slab is free of the metallic cover and in favor for the observation of eigen modes. To observe the corner modes, we implement the experiment with the microwave near-field scanning platform [Fig. 3(a)]. The setup includes a source antenna and a probe antenna connected to a vector network analyzer via a coaxial-cable. The probe antenna, mounted on an automatic stepper motor, collects signals at $z = 15$ mm, which are sent back to the vector network analyzer and a computer for imaging the eigen modes. The sample consists of periodic ceramic rods and two metallic bars, which are placed on the

metallic substrate. The corner of the sample is focused, and the source antenna is positioned at the center of four rods closest to the corner. We first consider the sample with $(\Delta x, \Delta y) = (-2$ mm, -4 mm$)$ to demonstrate the capability of imaging the eigen modes. The experimental $|E_z|^2$ fields of four representative eigen modes are shown in Fig. 3(b). At the frequency of 6.32 GHz, the bulk mode exhibits an extended field within the bulk PC slab. At 6.51 GHz, the y edge mode shows a confined field localized around the y edge, i.e., the boundary perpendicular to the y-axis. At 6.40 GHz, the mixed x & y edge mode exhibits an extended field along both the x and y edges. This is induced by the field overlapping between the x edge mode and the y edge mode at the same frequency (see details in Fig. 11 in Appendix C). Importantly, at 6.71 GHz, a strongly confined field localized at the corner is observed, confirming the existence of corner mode. To validate these experimental results, we also perform the full three-dimensional numerical simulation under the same excitation settings [Fig. 3(c)]. The simulated $|E_z|^2$ fields closely reproduce
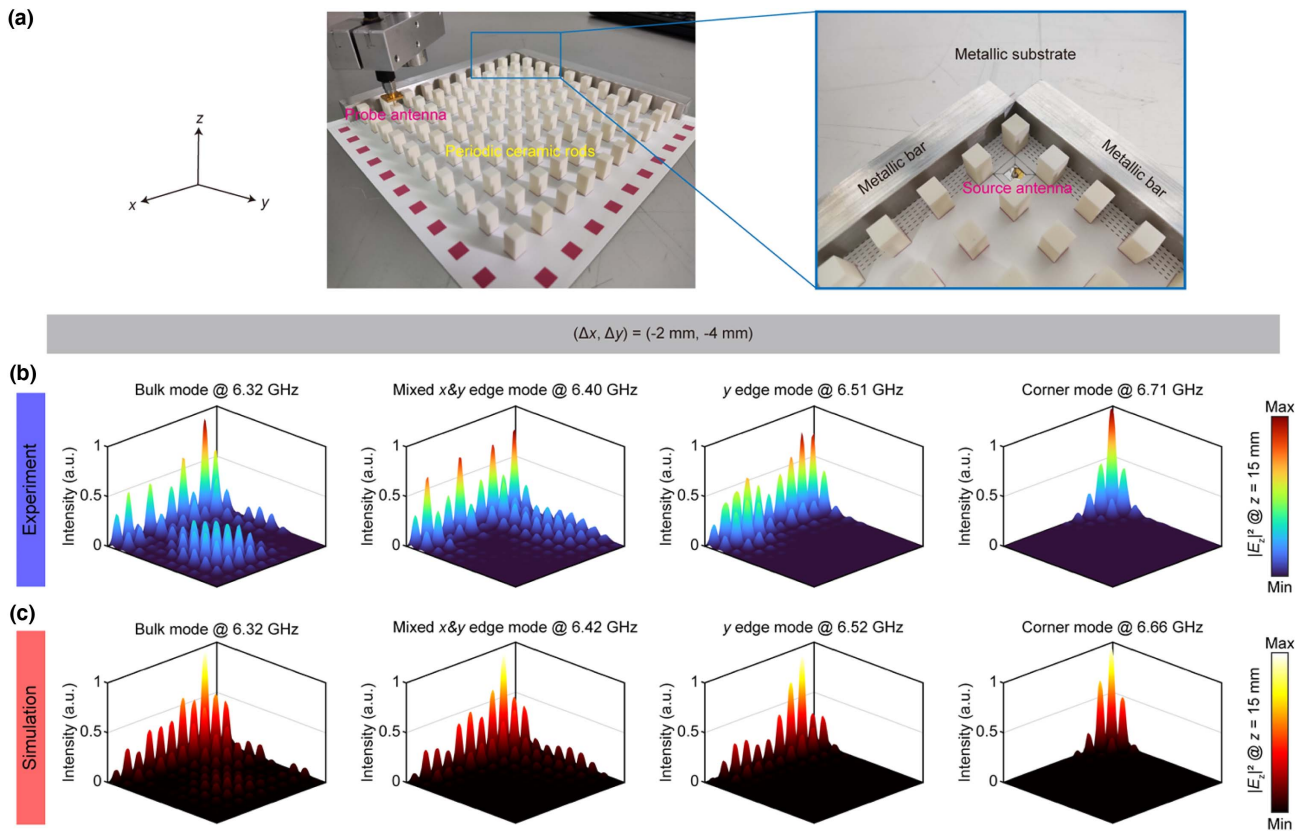
Fig. 3. Observation of eigen modes of the corner between the PC slab and two metallic bars. (a) Left panel: photograph of the fabricated experimental sample. Right panel: photograph of the corner of the sample. (b) Experimental $|E_z|^2$ fields at $z = 15$ mm of four eigen modes for the sample with $(\Delta x, \Delta y) = (-2$ mm, -4 mm), representing the bulk mode, the edge mode, and the corner mode. (c) Simulated $|E_z|^2$ fields of four representative eigen modes, which are consistent with the experimental results.

the experimental observations, providing further confirmation of the validity of the experimental results.

To further demonstrate the presence of gapless corner modes in synthetic translation dimensions, we perform measurements on samples with $\Delta x = \Delta y$. Since the source antenna is placed near the corner, there are field enhancements at frequencies where no eigen modes are expected. In order to accurately identify the resonantly excited corner modes, we define the response intensity $R = |E_z|^2_{corner}/|E_z|^2_{source}$, representing the ratio of the field intensity at the corner to that at the source. The positions of the corner and source are illustrated in the inset of Fig. 4(a). The response intensity reaches its maximum value when the corner mode is excited, and the peak of the response spectrum confirms the existence of the corner mode. Figure 4(a) shows the response intensity spectrum for the sample with $(\Delta x, \Delta y) = (-3$ mm, -3 mm), where the red line shows the simulated result and the blue shows the experimental result. The experimental and simulated frequencies of corner modes are 6.71 GHz and 6.70 GHz, respectively, demonstrating consistency between these two results. The measured and simulated $|E_z|^2$ fields of the excited corner modes for this sample are shown in Figs. 4(b) and 4(c), respectively, revealing a strongly localized field around the corner. Similarly, the response spectra, as well as the measured and simulated

$|E_z|^2$ fields, are presented for the sample with $(\Delta x, \Delta y) = (-4$ mm, -4 mm) in Figs. 4(d)–4(f), and for the sample with $(\Delta x, \Delta y) = (-5$ mm, -5 mm) in Figs. 4(g)–4(i). The frequencies of these corner modes are almost the same (with an error less than 0.8%), and the $|E_z|^2$ fields of these corner modes exhibit negligible differences, confirming the high consistency between the experimental and simulated results. By summarizing the results in Figs. 4(a), 4(d), and 4(g), we observe that the frequencies of corner modes increase from 6.71 GHz to 6.89 GHz and 7.17 GHz as $(\Delta x, \Delta y)$ changes from $(-3$ mm, -3 mm) to $(-4$ mm, -4 mm) and $(-5$ mm, -5 mm). When $(\Delta x, \Delta y) = (0$ mm$, 0$ mm) and $(-5.5$ mm, -5.5 mm), we observe the disappearance of the corner mode in the band gap (Fig. 12 in Appendix D). This provides clear evidence of the observation of gapless corner modes in synthetic translation dimensions.

Gapless corner modes can be employed to spatially separate topological corner modes. A recently published research work reported an acoustical topological rainbow by employing the same idea of translational deformation [59]. Similarly, we propose a photonic topological rainbow with gradient translation, taking advantage of the strong localization and gapless nature of corner modes in the PC slab. As shown in Fig. 5(a), we present a schematic illustration of the topological rainbow, which is
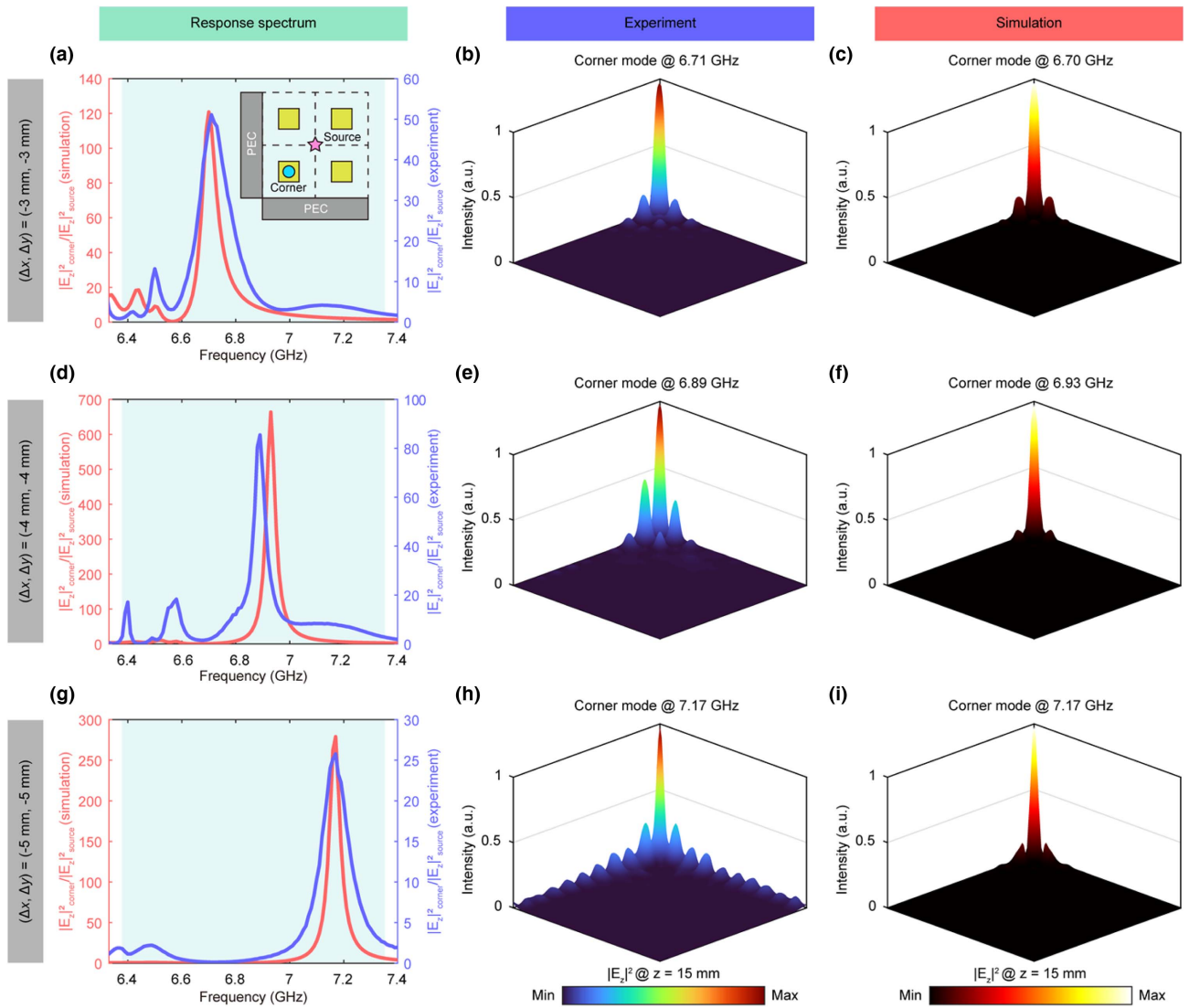
Fig. 4. Observation of gapless corner modes within the translation dimensions. (a) Response spectrum for the sample with $(\Delta x, \Delta y)$, = (–3 mm, –3 mm). The red line is the simulated result, and the blue is the experimental result. The cyan region represents band gap. The response intensity is defined as $|E_z|^2_{corner}/|E_z|^2_{source}$, whose peak indicates the excitation of corner mode. For the sample with $(\Delta x, \Delta y)$ = (–3 mm, –3 mm), the central frequencies of corner modes are 6.70 GHz (simulation) and 6.71 GHz (experiment). Inset: illustration of two positions at which electric field is used to determine the response intensity. (b), (c) Measured and simulated $|E_z|^2$ fields of the excited corner mode for the sample with $(\Delta x, \Delta y)$ = (–3 mm, –3 mm). (d)–(f) and (g)–(i) are similar to (a)–(c), while (d)–(f) correspond to the sample with $(\Delta x, \Delta y)$ = (–4 mm, –4 mm) and (g)–(i) correspond to the sample with $(\Delta x, \Delta y)$ = (–5 mm, –5 mm).

divided into six gradient regions (I, II, III, IV, V, VI) and one non-gradient region (VII). Region VII serves as a barrier region formed by OPC to provide a band gap preventing the leakage of light. In region I, there are a total of 5 × 5 dielectric rods. The dielectric rods in the first to fifth columns are translated by $(\Delta x_1, \Delta y_1)$, $(3\Delta x_1/4, 3\Delta y_1/4)$, $(\Delta x_1/2, \Delta y_1/2)$, $(\Delta x_1/4, \Delta y_1/4)$, and $(0, 0)$, respectively. This gradient architecture offers two advantages: first, the bottom-left corner of region I can be approximated to form a corner with translation $(\Delta x_1, \Delta y_1)$; second, the right side of region I can be considered as OPC to assist in forming the corner of the next region. Regions II, III, IV, V, VI are designed based on the similar principle. The $(\Delta x_n, \Delta y_n)$

(n = 1, 2, 3, 4, 5, 6) for the six gradient regions are (–6.5 mm, –6.5 mm), (7.5 mm, –7.5 mm), (–8.3 mm, –8.3 mm), (–8.9 mm, –8.9 mm), (–9.3 mm, –9.3 mm), and (–9.5 mm, –9.5 mm), respectively. They respectively support six corner modes of different frequencies. Consequently, when light is incident from the bottom, the frequency component around the frequency of the corner mode will be trapped in the corresponding corner, as shown in Fig. 5(b). Note that the variation of $(\Delta x_n, \Delta y_n)$ is not linear. Owing to the high quality factor of corner modes, we can effectively extract and separate two frequency components (7.28 and 7.34 GHz) with a frequency interval of 0.06 GHz into distinct spatial locations.
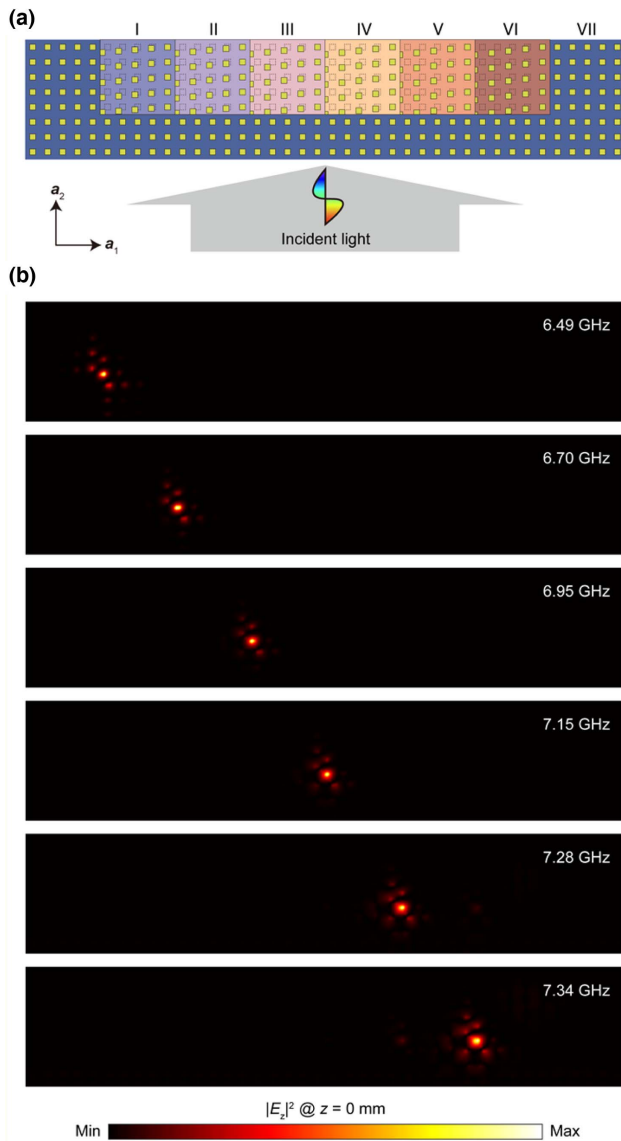
Fig. 5. Realization of photonic topological rainbow. (a) Schematic illustration of topological rainbow. (b) Calculated $|E_z|^2$ fields at $z = 0$ mm for different frequencies.

5. CONCLUSION

In contrast to previous works predominantly focused on the "corner mode in a single structure," this work delves into the "corner modes in multiple structures." Starting from the STPC, we find that topological corner modes exhibit robust gapless dispersion in synthetic translation dimensions and directly observe the gapless corner modes in PC slabs system. In dielectric photonic crystal, the breaking of chiral symmetry destroys the zero-energy character of the corner mode. Although it allows the corner mode to be embedded in bulk spectrum (manifested as BICs), the underlying mechanisms are different from the gapless corner modes. Utilizing the microwave near-field scanning platform, we map the mode evolution of the sample over a range of about 6–7 GHz from the bulk mode to the topological corner mode within the band gap. We verify the gapless characteristic of corner modes by translating rods and measuring response intensities. All measured results are in good agreement with the simulated results. The demonstrated gapless corner modes under synthetic translational deformations are universal and can be applied to other lattice structures. Our study demonstrates a feasible strategy for accessing and tuning topological corner modes at microwave frequencies. Although our implementation involved a metal-containing microwave system, it can be extended to nanophotonic systems working at optical frequencies. For example, the in-plane excitation of a topological corner mode at a telecommunications wavelength has been implemented by a cross-coupled PC cavity based on STPC [38]. Applying the same translation method to this nanophotonic structure, we can also observe the gapless corner modes at optical frequencies and further explore its applications in nonlinear optics and quantum optics.

APPENDIX A: TOPOLOGICAL NATURE OF GAPLESS CORNER MODES

Here, we discuss the topological nature of gapless corner modes. To begin with, we clarify the "translation" discussed in the main text. As shown in Fig. 6, left panel, we first present a perfect photonic crystal of square lattice, but it is divided into undeformed region (blue) and deformed region (orange). As shown in Fig. 6, right panel, we then apply
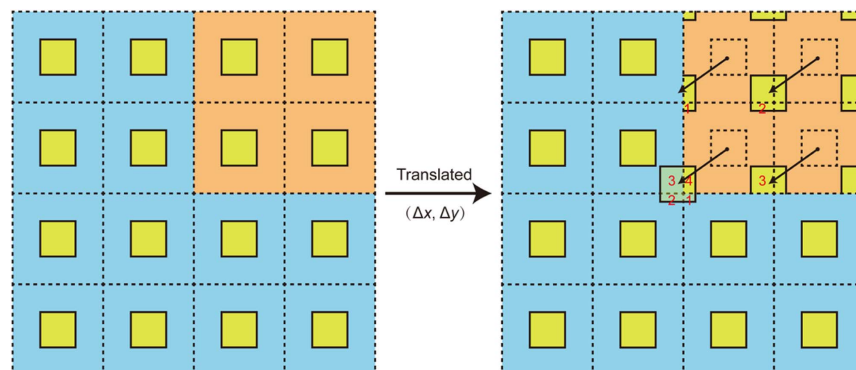

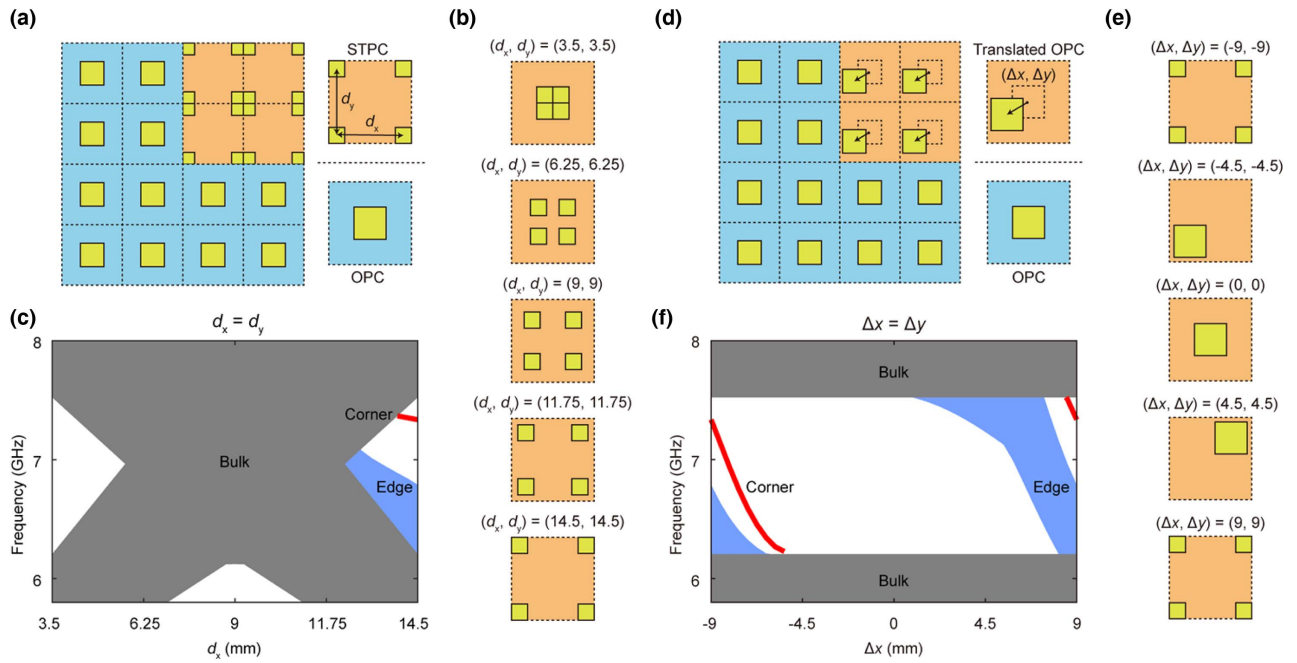**Fig. 6.** Schematic illustration of the translation of dielectric rods.

Fig. 7. Comparison of corner mode dispersions obtained by varying (d_x, d_y) or $(\Delta x, \Delta y)$. (a) Schematic illustration of the corner between the STPC and OPC. Here, d_x and d_y are varied as parameters, no longer fixed at $d_x = d_y = 14.5$ mm. (b) Schematic illustration of the unit cells of PC as (d_x, d_y) changes from (3.5 mm, 3.5 mm) to (14.5 mm, 14.5 mm). (c) Non-gapless dispersion of corner modes of configuration in (a) when $d_x = d_y$. (d) Schematic illustration of the corner between the translated OPC and the untranslated OPC [same as Fig. 1(c) in the main text]. (e) Schematic illustration of the unit cells of translated OPC as $(\Delta x, \Delta y)$ changes from (−9 mm, −9 mm) to (9 mm, 9 mm). (f) Gapless dispersion of corner modes of configuration in (d) when $\Delta x = \Delta y$ [same as Fig. 1(d) in the main text].

the same translation $(\Delta x, \Delta y)$ to each dielectric rod in the deformed region (expressed by the difference between the co-ordinates of the dielectric rod before and after the translation: $\Delta x = x_{\mathrm{deformed}} - x_{\mathrm{undeformed}}$, $\Delta y = y_{\mathrm{deformed}} - y_{\mathrm{undeformed}}$). The unit cells are fixed during the translation, while dielectric rods are translated by $(\Delta x, \Delta y)$ within their unit cell. When the translation is large enough, the dielectric rods intersect the boundary of their unit cell. The patch exiting one boundary re-enters through the corresponding periodic boundary, ensuring the integrity of the entire bulk crystal remains unchanged. For example, the patches 1, 2, 3 are moved out from the unit cell and seamlessly moved in through the corresponding periodic boundary.

As shown in Fig. 1, we show that such a translation acting as the synthetic translation dimensions can robustly ensure the gapless frequency shift of corner mode. In Figs. 7(a)–7(c), we present a counterexample to show that the gapless corner modes are not ubiquitous: we observe the frequency shift of corner mode by changing the in-plane distances d_x and d_y of the four square-rods and find that the frequency shift of the corner mode only covers part of the band gap when $d_x = d_y$. This situation is quite different from the gapless corner modes shown in Figs. 7(d)–7(f), i.e., Figs. 1(c) and 1(d) in the main text.

The nonzero second Chern number is calculated in the four-dimensional synthetic space by the Eq. (2), and the gapless corner modes can be understood through dimensional reduction. Specifically, when the translational invariances of k_x and k_y

are broken by truncated boundaries, the (4–2)-dimensional topological boundary modes in the $(\Delta x, \Delta y)$ space are triggered by bulk-edge correspondence, which are zero-dimensional corner modes in real space. Therefore, the existence of gapless corner modes is guaranteed in $(\Delta x, \Delta y)$ space. In Fig. 8, we show the frequency diagrams of the corner modes in $(\Delta x, \Delta y)$ space under the OPC and PEC boundary conditions, where the non-gray regions indicate the presence of corner modes. The frequencies of these corner modes are indicated by color, with blue indicating the lower bulk band edge frequency and red indicating the higher bulk band edge frequency. The transition from blue to red signifies the existence of gapless corner modes in $(\Delta x, \Delta y)$ space. The gapless dispersion of corner modes of $\Delta x = \Delta y$ (marked in diagonal dashed line) is shown in Figs. 1(d) and 1(f) in the main text.

We note that the frequency shift of the corner mode is a boundary effect but the gapless frequency shift is a topological effect. Therefore, we can insert air layers of different thicknesses weakening the boundary effect to verify that the gapless corner modes are not caused by the boundary effect, as shown in Fig. 9. It can be seen that the gapless corner modes persist with the increasing thickness of the air layer; however, the gap between the corner modes and edge modes diminishes until the corner modes fully degenerate into the edge modes. The disappearance of the corner modes is understandable because the air layer is not a good insulator for the electromagnetic waves. Otherwise, the gapless corner modes will persist regardless of the width of the inserted insulator.
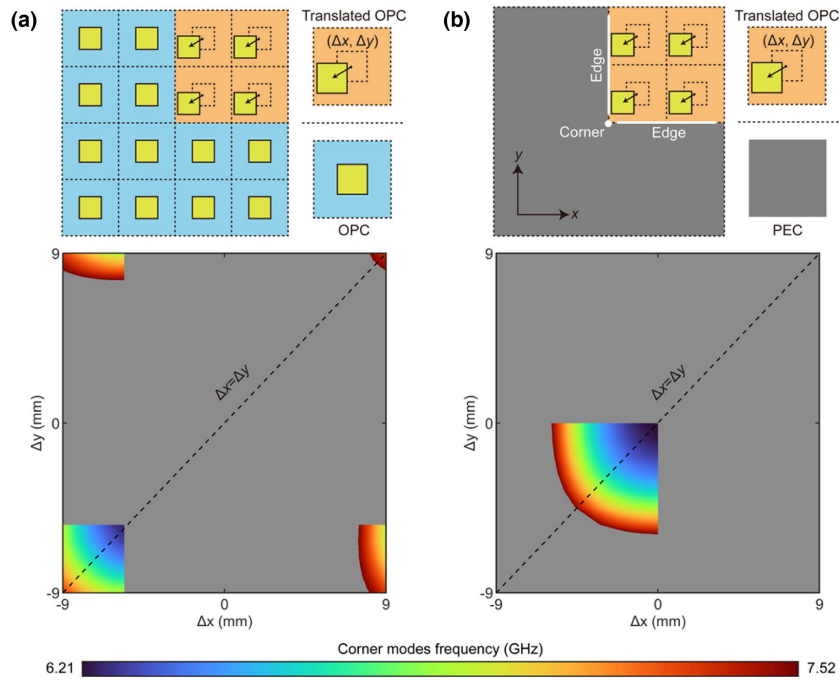
Fig. 8. Frequency diagrams of the corner modes in $(\Delta x, \Delta y)$ space. (a) Top panel, schematic illustration of the corner between the translated OPC and the untranslated OPC [same as Fig. 1(c)]. Bottom panel, frequency diagram of corner modes in $(\Delta x, \Delta y)$ space under the OPC boundary condition. (b) Top panel, schematic illustration of the corner between the translated OPC and PEC [same as Fig. 1(e) in the main text]. Bottom panel, frequency diagram of corner modes in $(\Delta x, \Delta y)$ space under the PEC boundary condition.
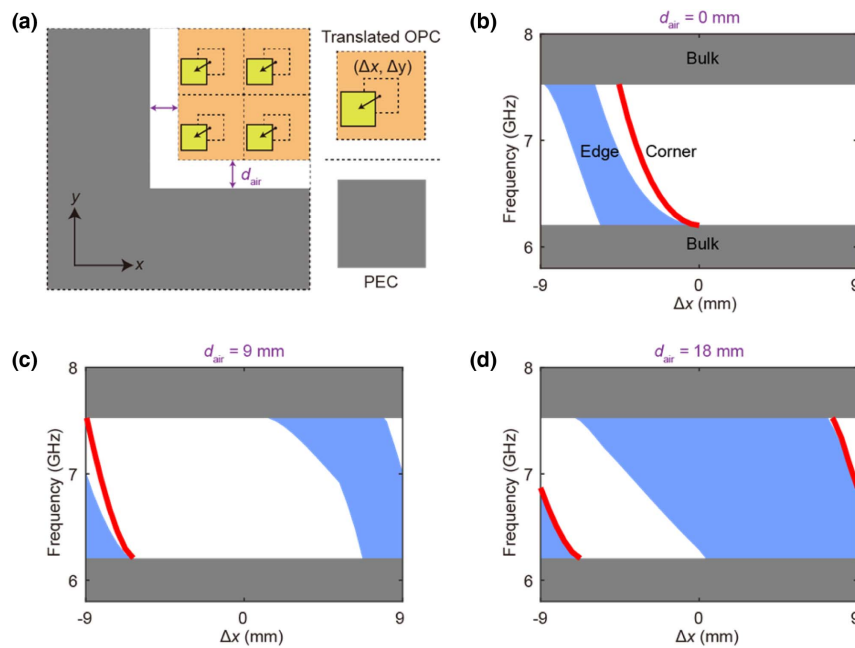

Fig. 9. Corner mode dispersion with inserted air layers of different thicknesses. (a) Schematic illustration of the corner with an inserted air layer between the translated OPC and PEC. The thickness of the air layer is denoted by d_{air}. (b) The gapless dispersion of corner modes with $d_{air} = 0$ mm. (c) The gapless dispersion of corner modes with $d_{air} = 9$ mm. (d) The gapless dispersion of corner modes with $d_{air} = 18$ mm.
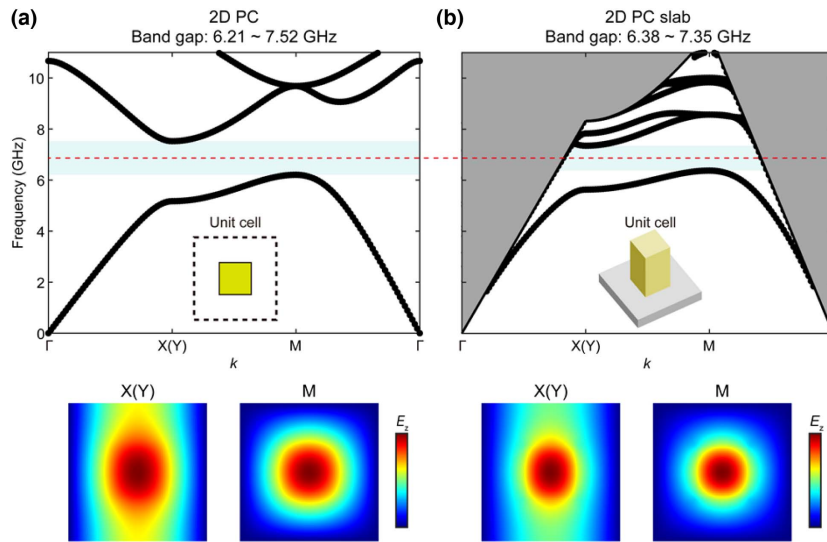
Fig. 10. Comparison of band structures and eigen fields of the 2D PC and 2D PC slab. (a) The band structure and eigen fields (the first band) of 2D PC, which is discussed in Fig. 1 in the main text. (b) The band structure and eigen fields (the first band) of 2D PC slab, which is applied in Figs. 2–5 in the main text.

APPENDIX B: THE PHOTONIC BAND STRUCTURE OF A PHOTONIC CRYSTAL SLAB

The results in Fig. 1 are based entirely on 2D PC. The experiments of the 2D PC require a metallic cover to prevent the radiation of electromagnetic waves into the free space. This metal cover not only complicates the experimental setup but also hinders the direct mapping of the electromagnetic field. Therefore, we propose the observation of gapless corner modes based on a PC slab consisting of dielectric rods placed on a perfect electrical conductor. As shown in Fig. 10, we simultaneously calculate the band structures and the eigen fields

(the first band) of the 2D PC and the PC slab. And both the band structures and eigen fields show the similarity between the 2D PC and the 2D PC slab, indicating the potential existence of gapless corner modes in the PC slab.

APPENDIX C: THE CLARIFICATION OF MIXED _X_ & _Y_ EDGE MODE

In Fig. 3, we experimentally observe the mixed x & y edge mode, which can be explained by the field overlapping between the x edge mode and the y edge mode at the same frequency. As shown in Fig. 11, we simulate the edge mode dispersion
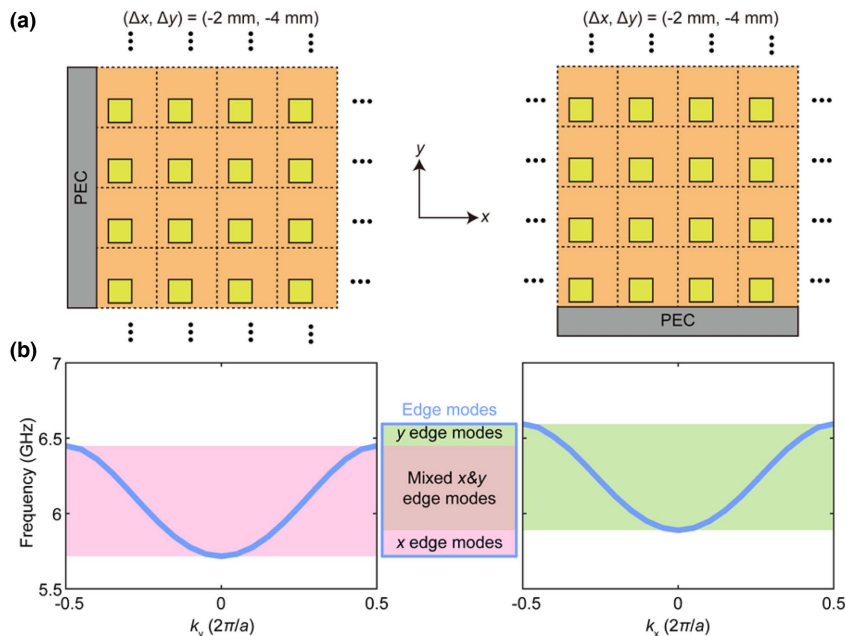

Fig. 11. Dispersion of x edge mode and y edge mode for the PC slab with $(\Delta x, \Delta y) = (-2 \text{ mm}, -4 \text{ mm})$. (a) 2D schematic illustrations of the edge between a metallic bar and the PC slab perpendicular to x and y axes, respectively. (b) The x edge mode and y edge mode dispersion.

in k_y and k_x directions of the PC slab with $(\Delta x, \Delta y) = (-2 \text{ mm}, -4 \text{ mm})$. The x edge mode decays in the x direction and propagates in the y direction, while the y edge mode exhibits the opposite behavior. The x edge mode and y edge mode dispersions are partially overlapped in the frequency domain. Since the properties of edge modes are solely determined by the corresponding boundary conditions, the x and y edge modes for the sample with $(\Delta x, \Delta y) = (-2 \text{ mm}, -4 \text{ mm})$ in the main text can be interpreted as a result of band projection of the x and y edge mode dispersion here along the k_y and k_x directions, respectively. This accounts for the observed mixed x & y edge mode and y edge mode in the experiment.

APPENDIX D: THE OBSERVATION OF GAPLESS CORNER MODES

Here, we demonstrate how the corner mode appears, moves, and disappears in the band gap as $(\Delta x, \Delta y)$ changes. As illustrated in Fig. 12, when $(\Delta x, \Delta y) = (0 \text{ mm}, 0 \text{ mm})$, the response intensity of the corner mode is nearly zero at all frequencies, confirming the absence of corner modes at this translation parameter. When $(\Delta x, \Delta y) = (-3 \text{ mm}, -3 \text{ mm})$, a peak of the response intensity appears at 6.71 GHz, indicating the emergence of corner mode within the band gap. Furthermore, when $(\Delta x, \Delta y)$ corresponds to $(-4 \text{ mm}, -4 \text{ mm})$ and $(-5 \text{ mm}, -5 \text{ mm})$, the peak values of the response intensity are 6.89 and 7.17 GHz, respectively, demonstrating the frequency shift of corner mode. Finally, when $(\Delta x, \Delta y) = (-5.5 \text{ mm}, -5.5 \text{ mm})$, the peak of the response intensity almost disappears, confirming that the corner modes are no longer within the band gap. These observations provide direct evidence for the existence of gapless corner modes in the PC slab.
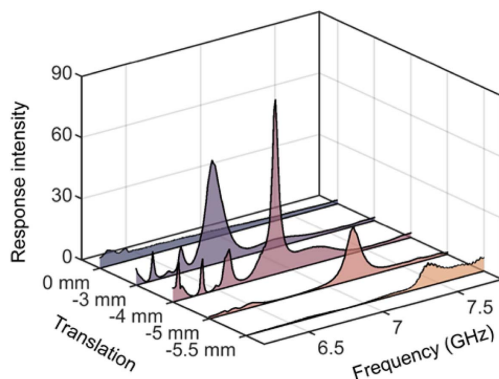
Fig. 12. Evolution of corner mode when $(\Delta x, \Delta y)$ changes.

REFERENCES

1. Y. Wu, C. Li, X. Hu, *et al.*, "Applications of topological photonics in integrated photonic devices," Adv. Opt. Mater. **5**, 1700357 (2017).
2. H. Xue, Y. Yang, and B. Zhang, "Topological valley photonics: physics and device applications," Adv. Photon. Res. **2**, 2100013 (2021).
3. H. Wang, S. K. Gupta, B. Xie, *et al.*, "Topological photonic crystals: a review," Front. Optoelectron. **13**, 50–72 (2020).
4. G. J. Tang, X. T. He, F. L. Shi, *et al.*, "Topological photonic crystals: physics, designs, and applications," Laser Photon. Rev. **16**, 2100300 (2022).
5. M. Segev and M. A. Bandres, "Topological photonics: where do we go from here?" Nanophotonics **10**, 425–434 (2020).
6. A. B. Khanikaev and G. Shvets, "Two-dimensional topological photonics," Nat. Photonics **11**, 763–773 (2017).
7. L. Lu, J. D. Joannopoulos, and M. Soljačić, "Topological photonics," Nat. Photonics **8**, 821–829 (2014).
8. T. Ozawa, H. M. Price, A. Amo, *et al.*, "Topological photonics," Rev. Mod. Phys. **91**, 015006 (2019).
9. Z. Chen and M. Segev, "Highlighting photonics: looking into the next decade," eLight **1**, 2 (2021).
10. T. Tian, Y. Zhang, L. Zhang, *et al.*, "Experimental realization of non-reciprocal adiabatic transfer of phonons in a dynamically modulated nanomechanical topological insulator," Phys. Rev. Lett. **129**, 215901 (2022).
11. M. Xiao, Z. Q. Zhang, and C. T. Chan, "Surface impedance and bulk band geometric phases in one-dimensional systems," Phys. Rev. X **4**, 021017 (2014).
12. Q. Yuan, L. Gu, L. Fang, *et al.*, "Giant enhancement of nonlinear harmonic generation in a silicon topological photonic crystal nanocavity chain," Laser Photon. Rev. **16**, 2100269 (2022).
13. M. Wang, R. Y. Zhang, L. Zhang, *et al.*, "Topological one-way large-area waveguide states in magnetic photonic crystals," Phys. Rev. Lett. **126**, 067401 (2021).
14. Q. Yang, D. Wang, S. Kruk, *et al.*, "Topology-empowered membrane devices for terahertz photonics," Adv. Photon. **4**, 046002 (2022).
15. H. Zhong, S. Xia, Y. Zhang, *et al.*, "Nonlinear topological valley Hall edge states arising from type-II Dirac cones," Adv. Photon. **3**, 056001 (2021).
16. T. Ma and G. Shvets, "All-Si valley-Hall photonic topological insulator," New J. Phys. **18**, 025012 (2016).
17. X.-D. Chen, F.-L. Zhao, M. Chen, *et al.*, "Valley-contrasting physics in all-dielectric photonic crystals: orbital angular momentum and topological propagation," Phys. Rev. B **96**, 020202 (2017).
18. C. A. Rosiek, G. Arregui, A. Vladimirova, *et al.*, "Observation of strong backscattering in valley-Hall photonic topological interface modes," Nat. Photonics **17**, 386–392 (2023).
19. M. Kim, Z. Jacob, and J. Rho, "Recent advances in 2D, 3D and higher-order topological photonics," Light Sci. Appl. **9**, 130 (2020).
20. B. Xie, H.-X. Wang, X. Zhang, *et al.*, "Higher-order band topology," Nat. Rev. Phys. **3**, 520–532 (2021).
21. W. A. Benalcazar, B. A. Bernevig, and T. L. Hughes, "Electric multipole moments, topological multipole moment pumping, and chiral Hinge states in crystalline insulators," Phys. Rev. B **96**, 245115 (2017).
22. W. A. Benalcazar, B. A. Bernevig, and T. L. Hughes, "Quantized electric multipole insulators," Science **357**, 61–66 (2017).
23. A. M. C. F. Schindler, M. G. Vergniory, Z. Wang, *et al.*, "Higher-order topological insulators," Sci. Adv. **4**, 6 (2018).
24. C. W. Peterson, W. A. Benalcazar, T. L. Hughes, *et al.*, "A quantized microwave quadrupole insulator with topologically protected corner states," Nature **555**, 346–350 (2018).

25. B.-Y. Xie, H.-F. Wang, H.-X. Wang, *et al.*, "Second-order photonic topological insulator with corner states," Phys. Rev. B **98**, 205147 (2018).

26. X. D. Chen, W. M. Deng, F. L. Shi, *et al.*, "Direct observation of corner states in second-order topological photonic crystal slabs," Phys. Rev. Lett. **122**, 233902 (2019).

27. S. Mittal, V. V. Orre, G. Zhu, *et al.*, "Photonic quadrupole topological phases," Nat. Photonics **13**, 692–696 (2019).

28. A. Dutt, M. Minkov, I. A. D. Williamson, *et al.*, "Higher-order topological insulators in synthetic dimensions," Light Sci. Appl. **9**, 131 (2020).

29. L. Zhang, Y. Yang, Z. K. Lin, *et al.*, "Higher-order topological states in surface-wave photonic crystals," Adv. Sci. **7**, 1902724 (2020).

30. X. Zhou, Z. K. Lin, W. Lu, *et al.*, "Twisted quadrupole topological photonic crystals," Laser Photon. Rev. **14**, 2000010 (2020).

31. M. Li, D. Zhirihin, M. Gorlach, *et al.*, "Higher-order topological states in photonic kagome crystals with long-range interactions," Nat. Photonics **14**, 89–94 (2019).

32. H.-X. Wang, L. Liang, B. Jiang, *et al.*, "Higher-order topological phases in tunable C_3 symmetric photonic crystals," Photon. Res. **9**, 1854–1864 (2021).

33. F. Liu and K. Wakabayashi, "Novel topological phase with a zero Berry curvature," Phys. Rev. Lett. **118**, 076803 (2017).

34. B. Y. Xie, G. X. Su, H. F. Wang, *et al.*, "Visualization of higher-order topological insulating phases in two-dimensional dielectric photonic crystals," Phys. Rev. Lett. **122**, 233903 (2019).

35. M.-C. Jin, Y.-F. Gao, H.-Z. Lin, *et al.*, "Corner states in second-order two-dimensional topological photonic crystals with reversed materials," Phys. Rev. A **106**, 013510 (2022).

36. Y. Chen, F. Meng, Z. Lan, *et al.*, "Dual-polarization second-order photonic topological insulators," Phys. Rev. Appl. **15**, 034053 (2021).

37. Y. Ota, F. Liu, R. Katsumi, *et al.*, "Photonic crystal nanocavity based on a topological corner state," Optica **6**, 786–789 (2019).

38. X.-T. He, M.-Y. Li, H.-Y. Qiu, *et al.*, "In-plane excitation of a topological nanophotonic corner state at telecom wavelengths in a cross-coupled cavity," Photon. Res. **9**, 1423–1431 (2021).

39. M. Jung, R. G. Gladstone, and G. B. Shvets, "Nanopolaritonic second-order topological insulator based on graphene plasmons," Adv. Photon. **2**, 046003 (2020).

40. H. R. Kim, M. S. Hwang, D. Smirnova, *et al.*, "Multipolar lasing modes from topological corner states," Nat. Commun. **11**, 5758 (2020).

41. W. Zhang, X. Xie, H. Hao, *et al.*, "Low-threshold topological nanolasers based on the second-order corner state," Light Sci. Appl. **9**, 109 (2020).

42. Y. Chen, Z. Lan, J. Li, *et al.*, "Topologically protected second harmonic generation via doubly resonant high-order photonic modes," Phys. Rev. B **104**, 155421 (2021).

43. S. S. Kruk, W. Gao, D. Y. Choi, *et al.*, "Nonlinear imaging of nanoscale topological corner states," Nano Lett. **21**, 4592–4597 (2021).

44. Z. Hu, D. Bongiovanni, D. Jukic, *et al.*, "Nonlinear control of photonic higher-order topological bound states in the continuum," Light Sci. Appl. **10**, 164 (2021).

45. X. Xie, W. Zhang, X. He, *et al.*, "Cavity quantum electrodynamics with second-order topological corner state," Laser Photon. Rev. **14**, 1900425 (2020).

46. X.-D. Chen, F.-L. Shi, J.-W. Liu, *et al.*, "Second Chern crystals with inherently nontrivial topology," Natl. Sci. Rev. **10**, nwac289 (2022).

47. L. Yuan, Q. Lin, M. Xiao, *et al.*, "Synthetic dimension in photonics," Optica **5**, 1396–1405 (2018).

48. T. Ozawa and H. M. Price, "Topological quantum matter in synthetic dimensions," Nat. Rev. Phys. **1**, 349–357 (2019).

49. E. Lustig and M. Segev, "Topological photonics in synthetic dimensions," Adv. Opt. Photon. **13**, 426–461 (2021).

50. M. Lohse, C. Schweizer, H. M. Price, *et al.*, "Exploring 4D quantum Hall physics with a 2D topological charge pump," Nature **553**, 55–58 (2018).

51. Q. Wang, M. Xiao, H. Liu, *et al.*, "Optical interface states protected by synthetic Weyl points," Phys. Rev. X **7**, 031032 (2017).

52. Z.-G. Chen, W. Zhu, Y. Tan, *et al.*, "Acoustic realization of a four-dimensional higher-order chern insulator and boundary-modes engineering," Phys. Rev. X **11**, 011016 (2021).

53. J. J. Liu, Z. W. Li, Z. G. Chen, *et al.*, "Experimental realization of Weyl exceptional rings in a synthetic three-dimensional non-Hermitian photonic crystal," Phys. Rev. Lett. **129**, 084301 (2022).

54. G. Li, L. Wang, R. Ye, *et al.*, "Direct extraction of topological Zak phase with the synthetic dimension," Light Sci. Appl. **12**, 81 (2023).

55. D. Yu, G. Li, L. Wang, *et al.*, "Moire lattice in one-dimensional synthetic frequency dimension," Phys. Rev. Lett. **130**, 143801 (2023).

56. D. Jukić and H. Buljan, "Four-dimensional photonic lattices and discrete tesseract solitons," Phys. Rev. A **87**, 013814 (2013).

57. Y. Nakata, Y. Ito, Y. Nakamura, *et al.*, "Topological boundary modes from translational deformations," Phys. Rev. Lett. **124**, 073901 (2020).

58. C. Lu, Y. Z. Sun, C. Wang, *et al.*, "On-chip nanophotonic topological rainbow," Nat. Commun. **13**, 2586 (2022).

59. D. Liao, Y. Liu, Z. Zhang, *et al.*, "Synthesizing topological acoustic rainbow trapping at deep-subwavelength corners," Sci. Bull. **68**, 1744–1747 (2023).

60. M. Mochol-Grzelak, A. Dauphin, A. Celi, *et al.*, "Efficient algorithm to compute the second Chern number in four dimensional systems," Quantum Sci. Technol. **4**, 014009 (2018).

61. S. V. Silva, D. E. Fernandes, T. A. Morgado, *et al.*, "Topological pumping and Tamm states in photonic systems," Phys. Rev. B **105**, 155133 (2022).